frontiers in Energy Research

ORIGINAL RESEARCH
published: 30 July 2020
doi: 10.3389/fenrg.2020.00182

Hybridizing δ-Type MnO_2 With Lignin-Derived Porous Carbon as a Stable Cathode Material for Aqueous Zn–MnO_2 Batteries

Weijun Zhou[1], Anran Wang[1], Aixiang Huang[1], Minfeng Chen[1], Qinghua Tian[2], Jizhang Chen[1,3] and Xinwu Xu[1,3]*

[1] College of Materials Science and Engineering, Nanjing Forestry University, Nanjing, China, [2] Department of Chemistry, School of Sciences, Zhejiang Sci-Tech University, Hangzhou, China, [3] Co-Innovation Center of Efficient Processing and Utilization of Forest Resources, Nanjing Forestry University, Nanjing, China

OPEN ACCESS

Edited by:
Dipan Kundu, University of New South Wales, Australia

Reviewed by:
Jiang Zhou, Central South University, China
Jian-Gan Wang, Northwestern Polytechnical University, China

***Correspondence:**
Jizhang Chen
jizhang.chen@hotmail.com

Specialty section:
This article was submitted to Electrochemical Energy Conversion and Storage, a section of the journal Frontiers in Energy Research

Received: 30 May 2020
Accepted: 10 July 2020
Published: 30 July 2020

Citation:
Zhou W, Wang A, Huang A, Chen M, Tian Q, Chen J and Xu X (2020) Hybridizing δ-Type MnO_2 With Lignin-Derived Porous Carbon as a Stable Cathode Material for Aqueous Zn–MnO_2 Batteries. Front. Energy Res. 8:182. doi: 10.3389/fenrg.2020.00182

With the advantages of intrinsic safety, low price, high output potential, and acceptable energy density, aqueous rechargeable Zn–MnO_2 batteries are gradually emerging as promising energy storage devices in recent years. Unfortunately, the structural instability and poor electrical conductivity of manganese dioxides still hinder their further applications. To tackle these issues, we demonstrate a high-performance cathode material for Zn–MnO_2 batteries by hybridizing lignin-derived porous carbon with δ-MnO_2 (denoted as LPC/δ-MnO_2). Benefiting from the high electrical conductivity of porous carbon, the LPC/δ-MnO_2 cathode material can offer high discharge capacity of 332.3 mAh g^{-1} at 0.2 A g^{-1} and excellent high-rate capability (196.1 mAh g^{-1} at 5 A g^{-1}). Meanwhile, the assembled Zn–MnO_2 battery displays good long-term cycling stability (82% capacity retention after 1000 cycles). Such superior performances are attributed to the synergetic effect of nanostructured δ-MnO_2 and porous carbon scaffold, which is in favor of rapid Zn^{2+} ion diffusion and large contribution ratio of pseudocapacitive Zn^{2+} ion intercalation. The results of this study show great prospects of hybridizing biomass-derived carbon framework with electrochemically active materials toward advanced energy storage materials.

Keywords: manganese dioxides, biomass-derived carbon, zinc-ion batteries, high-rate performances, aqueous energy storage

INTRODUCTION

Considering the growing demands for efficient and reliable energy storage devices in modern society, low-cost, good-safety, and long-lifespan rechargeable batteries are urgently needed. Despite the wide-range applications of lithium ion batteries (LIBs), LIBs still suffer from a series of problems because of the often-used organic electrolytes (Randau et al., 2020). Thus, it is extremely important

to develop alternative energy storage devices. Recently, aqueous zinc-ion batteries (AZIBs) have attracted significant attention, mainly attributed to the advantages of aqueous electrolytes and zinc metal anodes (Tang et al., 2019; Li et al., 2020). In particular, the zinc metal shows high theoretical capacity, adequate redox potential for aqueous energy storage, and high abundance with low cost (Wan et al., 2018; Wang et al., 2018). Moreover, the ionic radius of Zn^{2+} (0.74 Å) is smaller than that of Na^{+} (1.02 Å) and close to that of Li^{+} (0.69 Å) (Kundu et al., 2016; Zhang et al., 2017), making AZIBs a promising candidate for future energy storage devices. Actually, various suitable and advanced cathode materials such as MnO_2 polymorphs [e.g., α- (Gao X. et al., 2020), β- (Liu et al., 2019), γ- (Wang et al., 2020), and δ- (Nam et al., 2019)], vanadium-based oxides (Kundu et al., 2016; Soundharrajan et al., 2018), Prussian blue analogs (Zhang et al., 2015; Yang et al., 2019), and organic compounds (Guo et al., 2018; Tie et al., 2020) have been extensively explored.

As one of the most promising cathode materials, MnO_2 possesses the merits of low cost, high theoretical capacity (308 mAh g^{-1}, based on one electron reaction), high output voltage (∼1.4 V), and environmental friendliness (Jin et al., 2019; Zhang et al., 2019; Chen et al., 2020). Ever since Yamamoto et al. developed Zn//$ZnSO_4$//MnO_2 cell chemistry in 1986 for the first time, lots of impressive works have been dedicated to this field (Yamamoto and Shoji, 1986; Guo et al., 2020; Xie et al., 2020). For instance, Pan et al. (2016) studied the electrochemical performances of aqueous Zn//α-MnO_2 battery in a $ZnSO_4$ aqueous electrolyte with $MnSO_4$ additive and realized excellent rate capability and great cyclability (92% capacity retention after 5000 cycles. Zhong et al. (2020) recently proposed an electrolyte-decoupling strategy to widen the working potential of Zn-MnO_2 battery and achieved a large open-circuit voltage of 2.83 V as well as good cyclability. Among various crystallographic polymorphs of MnO_2, layered δ-type MnO_2 exhibits a relatively large interlayer spacing (about 0.7 nm in the (0 0 1) plane), enabling this type of material to be suitable for facile and reversible (de-)intercalation of Zn^{2+} ions (Wang et al., 2019a). However, as a semiconductor, MnO_2 has intrinsically poor conductivity (around 10^{-5} to 10^{-6} S cm^{-1}) that is not favorable for high-rate applications (Dong, 2019). To further optimize the electrical conductivity of MnO_2, various strategies have been developed, mostly through introducing conductive additives [such as graphene (Wu et al., 2018), carbon nanotubes (Zhang et al., 2019), and conductive polymers (Huang et al., 2018)]. For instance, Wu et al. (2018) proposed a graphene-coated α-MnO_2 as the cathode material for AZIBs. The graphene coating can not only reduce the dissolution of the MnO_2 during cycling, but also provide high connectivity for rapid ions/electrons transfer (Wu et al., 2018). However, it remains a great challenge to improve the electrical conductivity and stability of MnO_2 through a facile and cost-effective method.

Meaningfully, Lignin, as the second most abundant natural polymer, has been successfully demonstrated to be a viable precursor or feedstock for the energy storage devices, such as Li-ion batteries (Cao et al., 2019; Chinomso et al., 2019), Na-ion batteries (Lin et al., 2020), and supercapacitors (Wang et al., 2019d; Yu et al., 2019). Endowed with abundant aromatic polymer with a carbon content of about 60 wt.%, lignin is suitable for preparing porous carbon framework (Yu et al., 2019; Lin et al., 2020). Nevertheless, to the best of our knowledge, there have been no reports on lignin-derived carbon for AZIB storage systems (Yuan et al., 2019). Hence, it is highly meaningful to construct an integrated lignin-derived porous carbon (LPC) and MnO_2 nanocomposite with good electrical conductivity, superior structural stability, and satisfying electrochemical performances. In this work, we use a one-step hydrothermal method to combine δ-MnO_2 with LPC scaffold. The prepared LPC/δ-MnO_2 nanocomposite can provide considerably improved electrochemical performances compared to that of neat δ-MnO_2 sample. Impressively, the LPC/δ-MnO_2 cathode material shows a large reversible capacity of 332.3 mAh g^{-1} at 0.2 A g^{-1}, excellent rate capability of 196.1 mAh g^{-1} at a large current density of 5 A g^{-1}, and good cycling stability of 82% capacity retention over 1000 cycles, much better than that of δ-MnO_2 counterpart. Also, the pseudocapacitive Zn^{2+} ion intercalation occupies a large proportion of the total capacity of LPC/δ-MnO_2, e.g., 72.8% at 2.0 mV s^{-1}. Such great performances of LPC/δ-MnO_2 nanocomposite can be explained by the following reasons. Firstly, δ-MnO_2 active material with relatively large interlayer spacing (∼0.7 nm) can provide a fast Zn^{2+} transfer channel during charge/discharge processes. Secondly, the porous carbon skeleton ensures fast transmission of electrons, which improves the whole electrical conductivity. Thirdly, the porous carbon scaffold can help accommodate the volume change caused by the electrochemical redox reactions of MnO_2.

EXPERIMENT

Preparation of Neat δ-MnO_2

In a typical synthesis, 100 mL of 0.1 M $MnSO_4 \cdot H_2O$ aqueous solution was dropwise added into 100 mL of 0.1 M $K_2S_2O_8$ aqueous solution under stirring. After that, the mixed solution was stirred for 2 h. Next, 60 mL of 1.2 M NaOH aqueous solution was added slowly into the above-mentioned solution with stirring for another 1 h, followed by aging for 2 h in the air. The obtained precipitate was washed with de-ionized (DI) water and absolute ethanol for 6 times, and subsequently freeze-dried to obtain δ-MnO_2.

Preparation of Lignin-Derived Porous Carbon and LPC/δ-MnO_2 Nanocomposite

Lignin (de-alkaline) was purchased from Aladdin Chemicals, Shanghai, China. The LPC was prepared by ball milling and subsequent calcination process. In specific, 0.5 g lignin and 0.5 g K_2CO_3 (as the activating agent) were added with 3.0 g zirconia grinding balls into a zirconia grinding bowl. The mixture was then milled for six cycles (30-min run and 5-min rest, forward and reverse running) for a total effective ball grinding time of 180 minutes. The mixed powder was then carbonized at 800°C for 2 h under Ar atmosphere. Then, 2 M HCl aqueous solution

and sufficient DI water were used to wash the obtained black powder thoroughly. After drying, the LPC was obtained. For the synthesis of LPC/δ-MnO_2, 120.0 mg LPC and 252.9 mg $KMnO_4$ were added into 60 mL DI water. After that, the hydrothermal treatment was carried out at 140°C for 8 h. After being washed with DI water and ethanol and dried at 80°C for 12 h, the final product (LPC/δ-MnO_2) was obtained. For comparison, neat δ-MnO_2 without LPC was also prepared.

Characterization and Electrochemical Measurements

The morphology, structure, and chemical composition of samples were analyzed by field emission scanning electron microscope (FE-SEM, JEOL JSM-7600F), transmission electron microscope (TEM, JEOL JEM-2100F), powder X-ray diffractometer (XRD, Rigaku Ultima IV) with Cu Kα radiation source (λ = 1.5406 Å), X-ray photoelectron spectrometer (XPS, Kratos AXIS UltraDLD), elemental analyzer (Elementar Vario EL Cube), and N_2 adsorption/desorption analyzer (Quantachrome Autosorb-iQ2-MP). For the preparation of cathodes, 70% LPC/δ-MnO_2, 20% carbon black, and 10% polyvinylidene fluoride dispersed in N-methylpyrrolidone were coated onto Ti foils and then dried at 80°C for at least 6 h in an oven. After being pressed at 10 MPa, the Ti foils were sliced into rounds with 12 mm in diameter, serving as working electrodes. The mass loading of LPC/δ-MnO_2 is controlled at ∼1.25 mg cm^{-2}. The electrochemical performances of LPC/δ-MnO_2 were evaluated with CR2016-type coin cells, which were assembled using Zn foil as the counter/reference electrode, Whatman filter paper (GF/A) as the separator, and 2 M $ZnSO_4$/0.2 M $MnSO_4$ aqueous solution as the electrolyte. The Galvanostatic charge/discharge (GCD) measurements were performed on a LAND CT2001A instrument. Cyclic voltammetry (CV) and electrochemical impedance spectroscopy (EIS) measurements were carried out on a Bio-Logic VSP-300 electrochemical workstation.

RESULTS

The crystal structures of LPC, δ-MnO_2, and LPC/δ-MnO_2 were characterized by XRD measurements, and the results are shown in **Figure 1A**. The XRD pattern of LPC shows the broad peaks at around 23° and 43°, which are attributed to the crystallographic planes of (0 0 2) and (1 0 0) of graphitic carbon, respectively, indicating the pseudographitic structure in the carbon framework. The peaks at 30°, 43°, and 60° are indexed to the impurities of SiO_2 and Na_4SiO_4 from the carbonized lignin biomass. Besides, the characteristic diffraction peaks of neat δ-MnO_2 match with the standard PDF card (JCPDS 42-1317). As for the LPC/δ-MnO_2 nanocomposite, four peaks at around 12°, 24°, 36°, and 65° can be assigned to the (0 0 1), (0 0 2), (1 1 −1), and (3 1 −2) planes of birnessite-type MnO_2 with a layered structure (Liu et al., 2016; Chen Q. et al., 2018). In addition to δ-MnO_2, some other peaks in the LPC/δ-MnO_2 can be indexed to a hydrothermal by-product ($K_6Mn_2O_6$, JCPDS 36-0873). As shown in the insert of **Figure 1A**, in the crystal structure of δ-MnO_2, K^+ ions and H_2O molecules reside in the interlayer space of MnO_6 layers. The pre-intercalated K^+ ions and H_2O molecules can act as pillars to expand the interlayer distance and improve the structural stability (Wang et al., 2019b; Sun et al., 2020). The detailed valence states of Mn and C

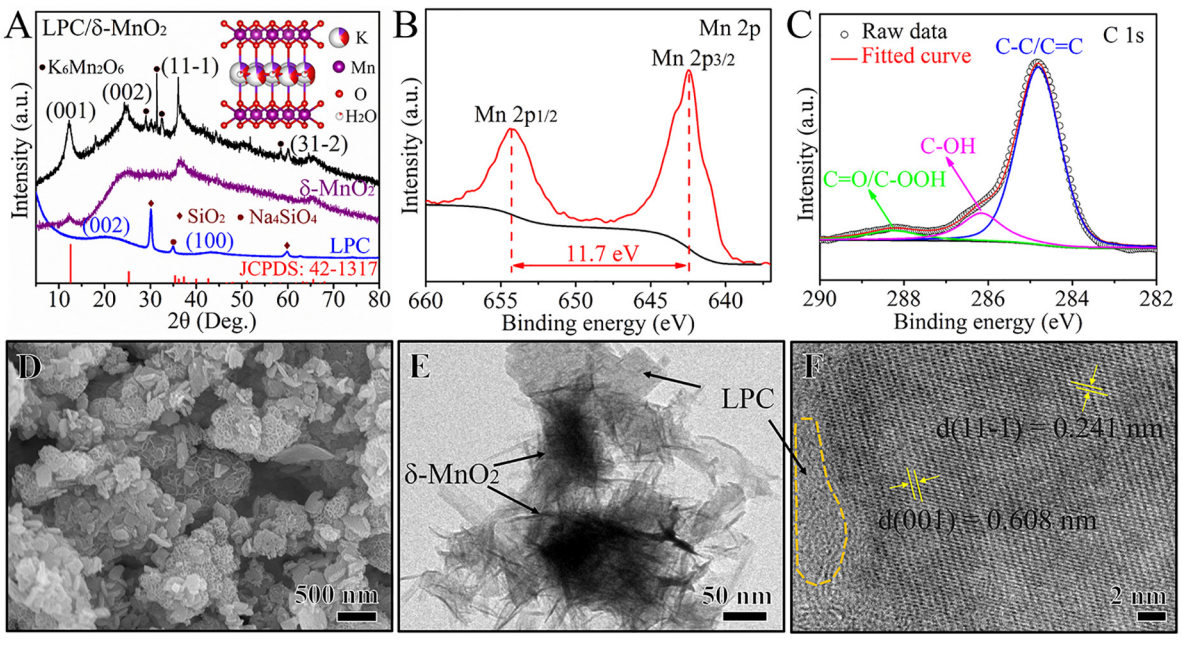

FIGURE 1 | (A) XRD patterns of LPC, δ-MnO_2, and LPC/δ-MnO_2 nanocomposite (the insert shows crystal structure of δ-MnO_2). **(B)** High-resolution Mn 2p, and **(C)** C 1s XPS spectra of LPC/δ-MnO_2. **(D)** SEM image, and **(E,F)** TEM images of LPC/δ-MnO_2.

elements were investigated through XPS analysis. As shown in **Figure 1B**, the high-resolution spectrum of Mn 2p can be split into two strong peaks situated at 654.3 and 642.5 eV, which are attributed to Mn $2p_{1/2}$ and $2p_{3/2}$, respectively. It should be noted that the spin-energy separation between $2p_{1/2}$ and $2p_{3/2}$ is 11.7 eV, revealing the presence of Mn^{4+} in LPC/δ-MnO_2 nanocomposite (Wang et al., 2019a). The XPS spectrum of C 1s in **Figure 1C** provides three subpeaks peaks, corresponding to C–C/C=C, C–OH, and C=O/C–OOH, respectively. Such rich oxygen-containing functional groups can make sure of good electrolyte wettability for the active material (Gao Q. et al., 2020). The LPC/δ-MnO_2 was further characterized by SEM and TEM techniques. As can be seen from **Figures 1D,E**, the surface of δ-MnO_2 is covered by LPC with a uniform dispersion state, and the LPC adopts two different morphologies, *i.e.*, nanoparticles and nanoplates. Such unique morphologies are beneficial to the penetration of Zn^{2+} ions and the exposure of sufficient active sites (Chen Q. et al., 2018). Meanwhile, the δ-MnO_2 with shape of homogenous flower-like morphology is composed of many curved nanosheets stacked in a cross way and the nanosheets have a thickness of about 50 nm. The HRTEM image in **Figure 1F** reveals the amorphous carbon region of LPC and two obvious lattice fringes of 0.608 and 0.241 nm, corresponding to the (0 0 1) and (1 1 −1) planes of δ-MnO_2, respectively. To further evaluate the structure of the LPC/δ-MnO_2, N_2 adsorption/desorption measurement was carried out. The Brunauer–Emmett–Teller (BET) specific surface area of LPC/δ-MnO_2 is calculated to be 39.89 $m^2\ g^{-1}$, providing sufficient channels for the facile infiltration of electrolyte. Based on the elemental analysis, the mass ratio of LPC in LPC/δ-MnO_2 nanocomposite is determined as 6.2%. Although the mass ratio of LPC is relatively low, it acts a pivotal part in enhancing electrochemical performances of LPC/δ-MnO_2 (Zhou et al., 2019). If the content of LPC is higher, the overall specific capacity of LPC/δ-MnO_2 would become lower.

As illustrated in the schematic diagram in **Figure 2A**, the electrochemical Zn^{2+} ion storage performances were investigated by using LPC/δ-MnO_2 nanocomposite, 2 M $ZnSO_4$/0.2 M $MnSO_4$ aqueous solution, and Zn foil as cathode material, electrolyte, and anode, respectively. High rate capability is critical for the practical applications of Zn–MnO_2 batteries. As can be seen from **Figure 2B**, at all the current densities,

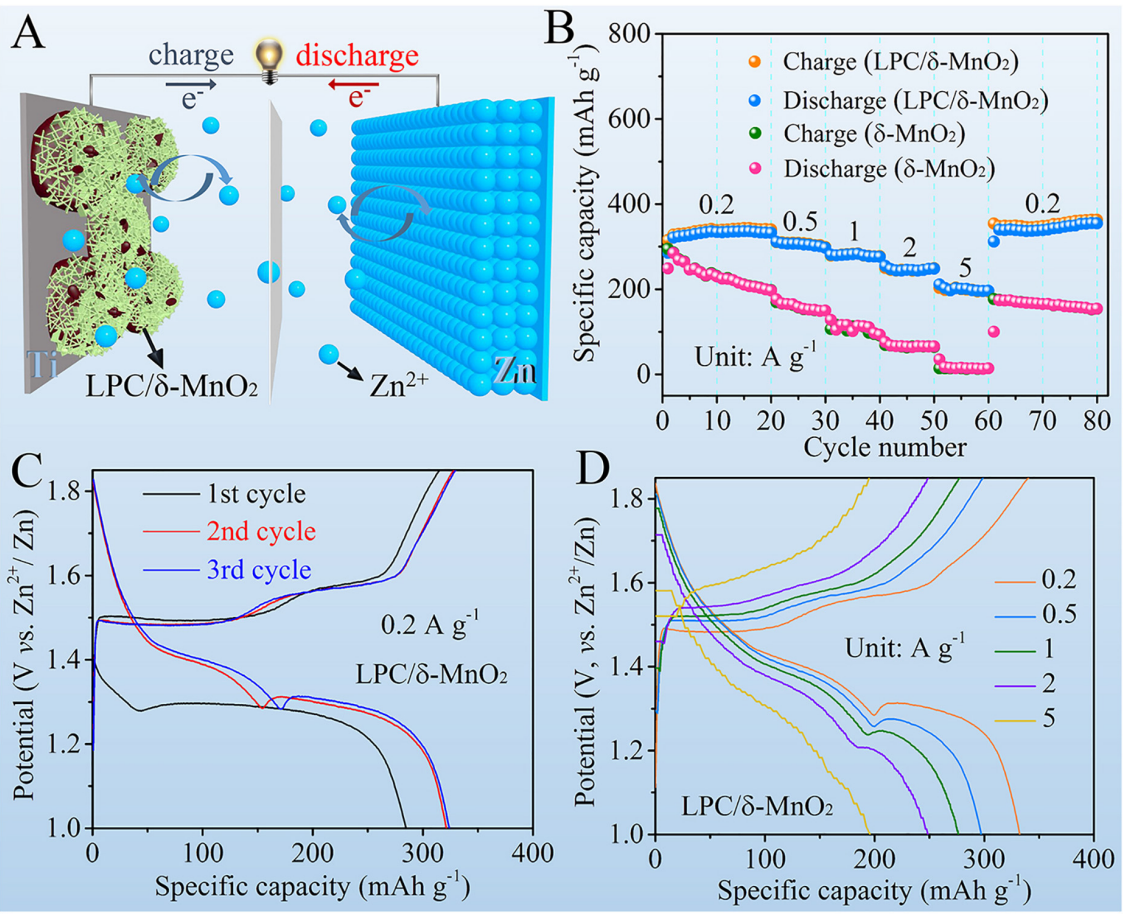

FIGURE 2 | (A) Schematic illustration of the Zn-MnO_2 battery with LPC/δ-MnO_2 cathode material. **(B)** Rate performances of LPC/δ-MnO_2 and δ-MnO_2. **(C)** GCD curves of LPC/δ-MnO_2 at the initial three cycles at 0.2 A g^{-1}. **(D)** GCD curves of LPC/δ-MnO_2 at different current densities.

the LPC/δ-MnO_2 nanocomposite exhibits much higher capacities than that of the neat δ-MnO_2. As the current density increases from 0.2 A g^{-1} gradually, the discharge capacity of LPC/δ-MnO_2 at the end of each current density declines from 332.3 to 297.1, 276.2, 248.5, and 196.1 mAh g^{-1} at 0.5, 1, 2, and 5 A g^{-1}, respectively. In addition, when recovering to 0.2 A g^{-1}, the discharge capacity of LPC/δ-MnO_2 can return to a high value of 339.1 mAh g^{-1}, showing good reversibility of the LPC/δ-MnO_2 nanocomposite. However, in sharp contrast, the capacity of δ-MnO_2 is 196.8 mAh g^{-1} at 0.2 A g^{-1}, which falls rapidly to 149.9, 93.1, and 65.7 mAh g^{-1} at 0.5, 1, and 2 A g^{-1}, respectively. Worse still, merely 14.1 mAh g^{-1} is maintained at a relatively large current density of 5 A g^{-1}, manifesting the extremely poor rate performances of pure MnO_2 material (Xu et al., 2019). **Figure 2C** presents the GCD curves of LPC/δ-MnO_2 in initial three cycles at 0.2 A g^{-1}. It is seen that the LPC/δ-MnO_2 gives an initial discharge capacity of 284.7 mAh g^{-1}, which rises to 321.2 and 324.0mAh g^{-1} at the 2nd and 3rd cycles, respectively. The increasement in capacity is attributed to the gradual activation of manganese oxide materials and similar phenomenon has been shown in previous reports (Liu et al., 2019; Zhang et al., 2019; Gao Q. et al., 2020). **Figure 2D** shows the corresponding GCD profiles of LPC/δ-MnO_2 at current densities ranging from 0.2 to 5 A g^{-1}. The curve profiles manifest nearly the same shape and small electrochemical polarization at different rates, implying fast charge transfer kinetics. Notably, the capacity fading along with the increased current density mainly comes from the shrinkage of the second discharge plateau. These results highlight the significant structural stability of the Zn–MnO_2 battery in delivering high capacities at various currents (Pan et al., 2016; Huang et al., 2018; Gao X. et al., 2020).

Cycling stability is a vital criterion for Zn–MnO_2 batteries. As shown in **Figure 3A**, at a low current density of 0.2 A g^{-1}, the LPC/δ-MnO_2 exhibits discharge capacities of 282.1 and 329.1 mAh g^{-1} for the initial two cycles. After 300 cycles, the capacity declines to 292.5 mAh g^{-1} gradually, corresponding to a high capacity retention of 89% (compared with the second cycle). Instead, when LPC is not employed, neat δ-MnO_2 only provides 215.5 and 253.3 mAh g^{-1} for the initial two cycles. After 300 cycles, the capacity of neat δ-MnO_2 drops

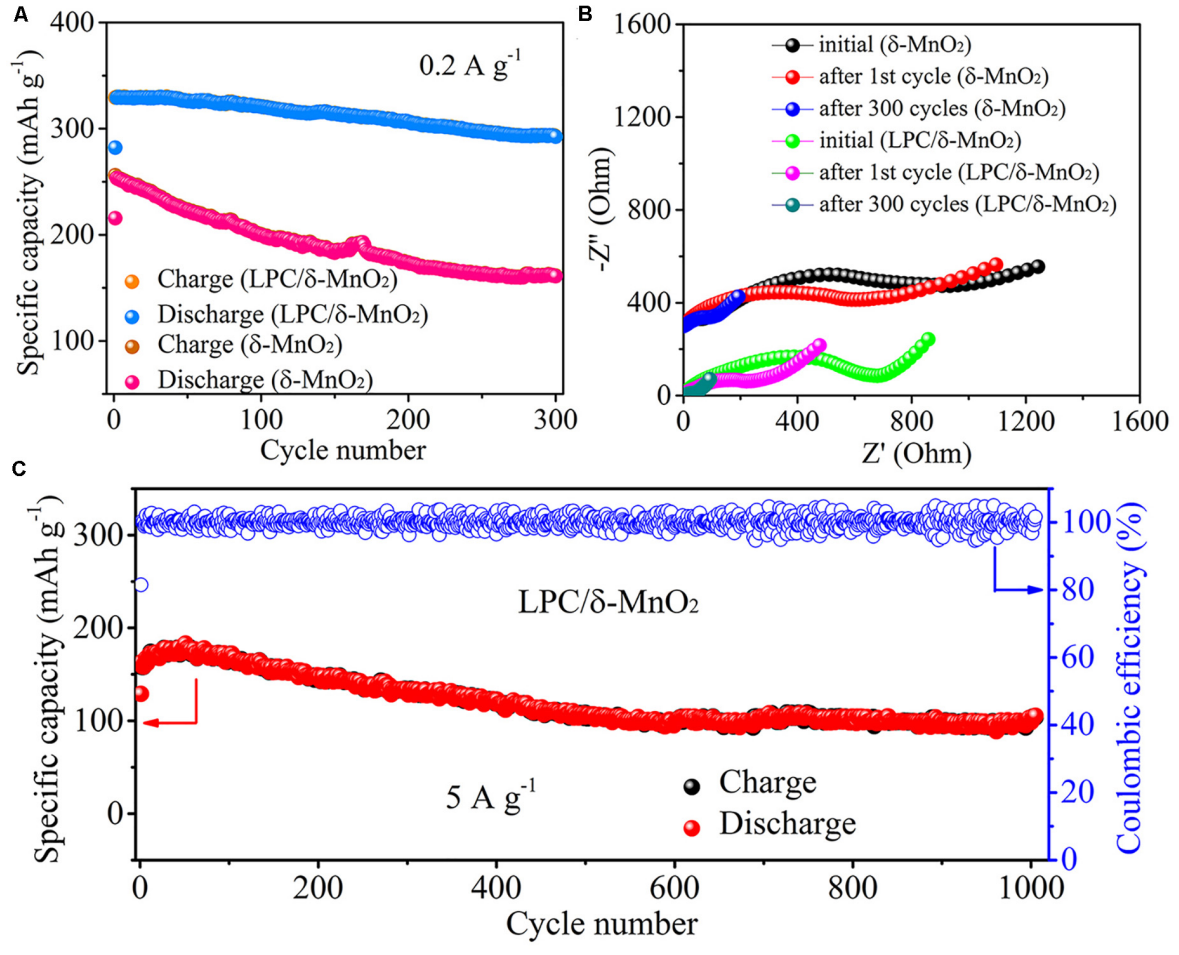

FIGURE 3 | (A) Cycling performances of LPC/δ-MnO_2 and δ-MnO_2 at 0.2 A g^{-1}. **(B)** Nyquist plots of the Zn–MnO_2 batteries with LPC/δ-MnO_2 and δ-MnO_2 at different states during cycling. **(C)** Long-term cycling performances of LPC/δ-MnO_2 at 5 A g^{-1}.

rapidly to 160.9 mAh g^{-1}, showing inferior cyclability (64% capacity retention). These results further indicate that the LPC framework plays an important role in stabilizing the electrochemical properties of δ-MnO_2. At the same time, in order to obtain more information about the electrochemical kinetics of LPC/δ-MnO_2, the EIS measurements were carried out using 5 mV amplitude with frequency ranging from 10 mHz to 100 kHz during the cycling process. The Nyquist plots of LPC/δ-MnO_2 and δ-MnO_2 are shown in **Figure 3B**. All the EIS curves show depressed semicircles in the high frequency region and sloped lines at low frequencies. Generally, the semicircle reflects charge transfer resistance (R_{ct}), while the sloped line is ascribed to ion diffusion in the bulk electrodes (Chen J. et al., 2018; Chen Y. et al., 2019; Hao et al., 2019; Xu et al., 2019). It is found that the R_{ct} values of LPC/δ-MnO_2 are smaller than that of δ-MnO_2 at different states during the whole cycling test, indicating better electrochemical kinetics of LPC/δ-MnO_2. In detail, at the initial state, the R_{ct} value of LPC/δ-MnO_2 is 681.2 Ω. After the 1st and 300th cycles, the R_{ct} decreases to 229.2 and 39.8 Ω, respectively. In contrast, the R_{ct} of δ-MnO_2 at different states are much higher (947.3 Ω at initial state, 610.9 Ω after 1st cycle, and 99.4 Ω after 300th cycle). The EIS results demonstrate that the charge transfer kinetics is improved and the electrochemical activity is enhanced when δ-MnO_2 is modified by LPC networks. The long-term cycling stability of LPC/δ-MnO_2 was further tested at 5 A g^{-1} (**Figure 3C**). Even after 1000 cycles, a high reversible capacity of 105.4 mAh g^{-1} is retained. Moreover, the coulombic efficiencies (CE) approach 100% after the 1st cycle, displaying good reversibility and excellent long-term cycling stability. These results further confirm that utilizing LPC as conductive framework and structural stabilizer for Mn-based cathode materials can substantially improve the performances of Zn–MnO_2 batteries in terms of rate capability and cyclability.

The electrochemical redox behaviors were further investigated by CV tests from 1.0 to 1.85 V. **Figure 4A** depicts the CV curves of LPC/δ-MnO_2 at initial six cycles at 0.2 mV s^{-1}. Obviously, there are two well separated reduction peaks at around 1.37 and 1.26 V (vs. Zn^{2+}/Zn) on cathodic sweeping, corresponding to the insertion processes of H^+ and Zn^{2+}, respectively

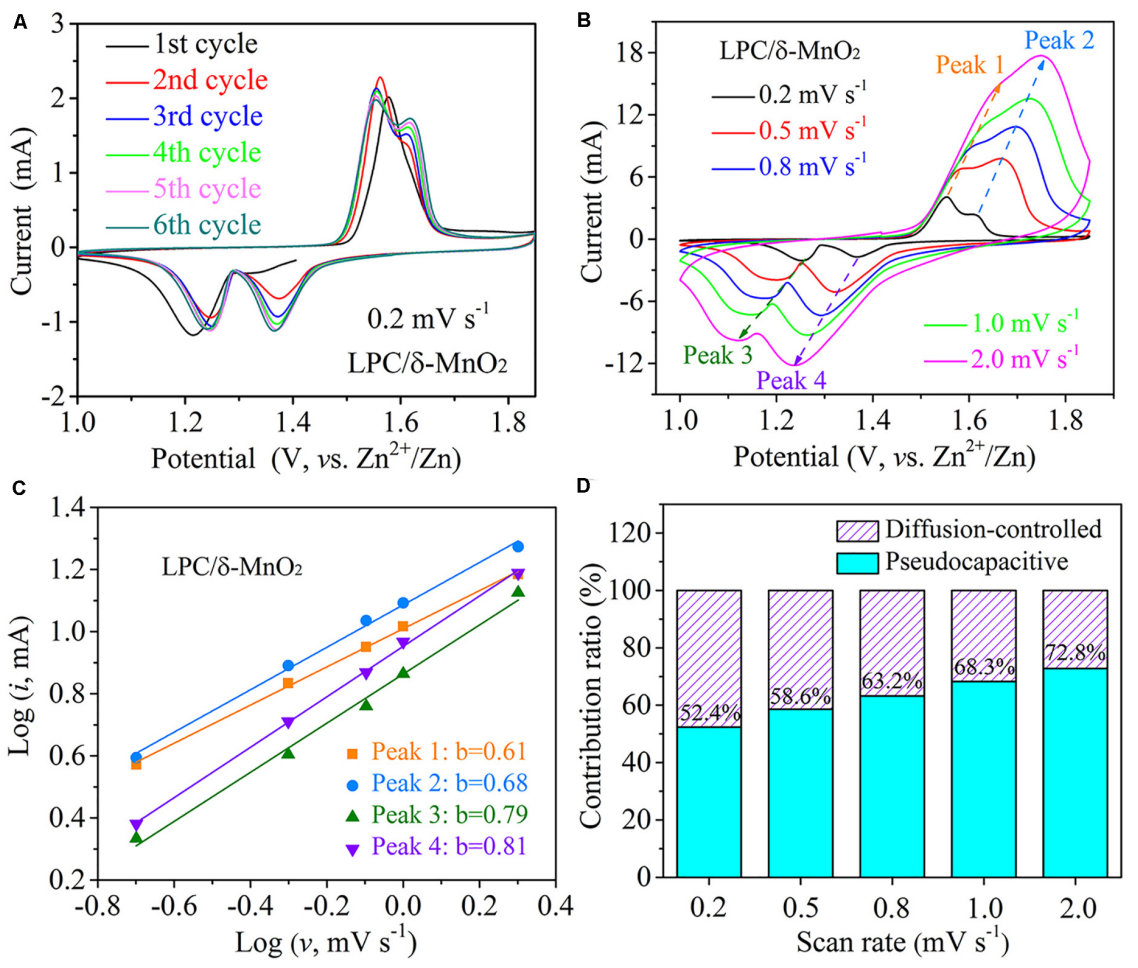

FIGURE 4 | (A) CV curves of LPC/δ-MnO_2 in initial six cycles at 0.2 mV s^{-1}. **(B)** CV curves of LPC/δ-MnO_2 at scan rates from 0.2 to 2.0 mV s^{-1}. **(C)** Log (*i*) vs. log (v) for different redox peaks in the CV curves. **(D)** Contribution ratios of diffusion-controlled and pseudocapacitive capacities of LPC/δ-MnO_2 at different scan rates.

(Wang et al., 2019c; You et al., 2020). Besides, it is found that the average peak current has no obvious loss in the initial six cycles, indicative of excellent electrochemical reversibility. CV measurements at different scan rates from 0.2 to 2.0 mV s^{-1} were also carried out to analyze the Zn–MnO_2 battery with LPC/δ-MnO_2 nanocomposite cathode material. As shown in **Figure 4B**, as the scan rate increases, the anodic peaks shift to higher potential, while the cathodic peaks move to lower potential at the same time. When the scan rate increases to a larger degree, these CV peaks get broader gradually. This phenomenon is due to the increased electrochemical polarization at a higher scan rate (Wang et al., 2019c). Based on the empirical power-law relationship between the peak current (i) and scan rate (ν), the following equation is used (Augustyn et al., 2013):

$$i = a\nu^b \tag{1}$$

Here, a and b are variable parameters (Zhou et al., 2019). According to the slop of log (i) vs. log (ν) in **Figure 4C**, the b values associated with four redox peaks are 0.61, 0.68, 0.79, and 0.81, respectively, suggesting that the capacitive intercalation behaviors dominate the corresponding redox reactions in Zn–MnO_2 batteries. In addition, i(V), the current response, can be quantitatively separated into capacitive ($k_1\nu$) and diffusion-controlled ($k_2\nu^{1/2}$) parts based on the following equation (Ming et al., 2018; Chen L. et al., 2019; Han et al., 2020):

$$i(V) = k_1\nu + k_2\nu^{1/2} \tag{2}$$

By determining the k_1 parameter, the capacitive contribution can be calculated. As illustrated in **Figure 4D**, when the scan rate increases from 0.2 to 2.0 mV s^{-1}, the capacitive contribution ratio rises from 52.4 to 72.8% gradually. That is, considerable portion of pseudocapacitive intercalation takes part in the Zn^{2+} ion storage process, especially at high rates. Hence, it is not surprising that the LPC/δ-MnO_2 shows great rate capabilities in **Figure 2B**.

CONCLUSION

Benefiting from large specific capacity and high output potential, MnO_2 has received great attention as the cathode material for AZIBs. However, the bottleneck of MnO_2 is severe capacity fading and structural instability during cycling. In this study, the LPC/δ-MnO_2 nanocomposite with enhanced structural stability and improved electrical conductivity is constructed through a facile hydrothermal method. At 0.2 A g^{-1}, the LPC/δ-MnO_2 delivers a high specific capacity of 332.3 mAh g^{-1}, 74.8 and 59.0% of which can be retained when the current density is as high as 2 and 5 A g^{-1}, respectively. Moreover, the capacity retention of LPC/δ-MnO_2 can reaches 82% over a long term of 1000 cycles. Such great performances are attributed to the large specific surface area, low charge transfer impedance, and large contribution ratio of pseudocapacitive Zn^{2+} ion intercalation. In short, this study not only offers new insights into enhancing the performances of MnO_2 for AZIBs but also put forwards a novel strategy for exploring low-cost biomass-derived porous carbon for advanced energy storage devices.

DATA AVAILABILITY STATEMENT

The original contributions presented in the study are included in the article/supplementary material, further inquiries can be directed to the corresponding author.

AUTHOR CONTRIBUTIONS

All authors extensively discussed the results, reviewed the manuscript, and approved the final version of the manuscript to be published.

FUNDING

This work was financially supported by the National Natural Science Foundation of China (No. 51902165), the Program of High-Level Talents in Six Industries of Jiangsu Province (No. XCL-040), the Natural Science Foundation of Jiangsu Province (No. BK20170917), and the Jiangsu Specially Appointed Professor Program.

REFERENCES

Augustyn, V., Come, J., Lowe, M. A., Kim, J. W., Taberna, P. L., Tolbert, S. H., et al. (2013). High-rate electrochemical energy storage through Li+ intercalation pseudocapacitance. *Nat. Mater.* 12, 518–522. doi: 10.1038/nmat3601

Cao, D., Zhang, Q., Hafez, A. M., Jiao, Y., Ma, Y., Li, H., et al. (2019). Lignin-derived holey, layered, and thermally conductive 3D scaffold for lithium dendrite suppression. *Small Methods* 3:1800539. doi: 10.1002/smtd.201800539

Chen, J., Fang, K., Chen, Q., Xu, J., and Wong, C.-P. (2018). Integrated paper electrodes derived from cotton stalks for high-performance flexible supercapacitors. *Nano Energy* 53, 337–344. doi: 10.1016/j.nanoen.2018.08.056

Chen, Q., Chen, J., Zhou, Y., Song, C., Tian, Q., Xu, J., et al. (2018). Enhancing pseudocapacitive kinetics of nanostructured MnO2 through anchoring onto biomass-derived porous carbon. *Appl. Surf. Sci.* 440, 1027–1036. doi: 10.1016/j.apsusc.2018.01.224

Chen, L., Ruan, Y., Zhang, G., Wei, Q., Jiang, Y., Xiong, T., et al. (2019). Ultrastable and high-performance Zn/VO2 battery based on a reversible single-phase reaction. *Chem. Mater.* 31, 699–706. doi: 10.1021/acs.chemmater.8b03409

Chen, Y., Zhou, L., Chen, L., Duan, G., Mei, C., Huang, C., et al. (2019). Anisotropic nanocellulose aerogels with ordered structures fabricated by directional freeze-drying for fast liquid transport. *Cellulose* 26, 6653–6667. doi: 10.1007/s10570-019-02557-z

Chen, M., Zhou, W., Wang, A., Huang, A., Chen, J., Xu, J., et al. (2020). Anti-freezing flexible aqueous Zn-MnO2 batteries working at -35°C enabled by a borax-crosslinked polyvinyl alcohol/glycerol gel electrolyte. *J. Mater. Chem. A* 8, 6828–6841. doi: 10.1039/d0ta01553a

Chinomso, M. E., Liu, X., Wu, M., and Yong, H. (2019). Lignin-containing cellulose nanomaterials: A promising new nanomaterial for numerous applications. *J. Bioresour. Bioprod.* 4, 3–10. doi: 10.21967/jbb.v4i1.186

Dong, D. (2019). Ternary composite MnO2@MoS2/Polypyrrole from in-situ synthesis for binder-free and flexible supercapacitor. *J. Bioresour. Bioprod.* 4, 242–250. doi: 10.12162/jbb.v4i4.010

Gao, Q., Li, D., Liu, X., Wang, Y., Liu, W., Ren, M., et al. (2020). Biomass-derived mesoporous carbons materials coated by α-Mn3O4 with ultrafast zinc-ion diffusion ability as cathode for aqueous zinc ion batteries. *Electrochim. Acta* 335:135642. doi: 10.1016/j.electacta.2020.135642

Gao, X., Wu, H., Li, W., Tian, Y., Zhang, Y., Wu, H., et al. (2020). H(+)-insertion boosted alpha-MnO2 for an aqueous Zn-ion battery. *Small* 16:1905842. doi: 10.1002/smll.201905842

Guo, X., Zhou, J., Bai, C., Li, X., Fang, G., and Liang, S. (2020). Zn/MnO2 battery chemistry with dissolution-deposition mechanism. *Mater. Today Energy* 16:100396. doi: 10.1016/j.mtener.2020.100396

Guo, Z., Ma, Y., Dong, X., Huang, J., Wang, Y., and Xia, Y. (2018). An environmentally friendly and flexible aqueous zinc battery using an organic cathode. *Angew. Chem. Int. Edit.* 57, 11737–11741. doi: 10.1002/anie.201807121

Han, X., Zhang, Z., Chen, S., and Yang, Y. (2020). Low temperature growth of graphitic carbon on porous silicon for high-capacity lithium energy storage. *J. Power Sources* 463, 228245–228253. doi: 10.1016/j.jpowsour.2020.228245

Hao, J., Long, J., Li, B., Li, X., Zhang, S., Yang, F., et al. (2019). Toward high-performance hybrid Zn-based batteries via deeply understanding their mechanism and using electrolyte additive. *Adv. Funct. Mater.* 29:1903605. doi: 10.1002/adfm.201903605

Huang, J., Wang, Z., Hou, M., Dong, X., Liu, Y., Wang, Y., et al. (2018). Polyaniline-intercalated manganese dioxide nanolayers as a high-performance cathode material for an aqueous zinc-ion battery. *Nat. Commun.* 9:2906. doi: 10.1038/s41467-018-04949-4

Jin, Y., Zou, L., Liu, L., Engelhard, M. H., Patel, R. L., Nie, Z., et al. (2019). Joint charge storage for high-rate aqueous zinc-manganese dioxide batteries. *Adv. Mater.* 31:1900567. doi: 10.1002/adma.201900567

Kundu, D., Adams, B. D., Duffort, V., Vajargah, S. H., and Nazar, L. F. (2016). A high-capacity and long-life aqueous rechargeable zinc battery using a metal oxide intercalation cathode. *Nat. Energy* 1:16119. doi: 10.1038/nenergy.2016.119

Li, C., Xie, X., Liang, S., and Zhou, J. (2020). Issues and future perspective on zinc metal anode for rechargeable aqueous zinc-ion batteries. *Energy Environ. Mater.* 3, 146–159. doi: 10.1002/eem2.12067

Lin, X., Liu, Y., Tan, H., and Zhang, B. (2020). Advanced lignin-derived hard carbon for Na-ion batteries and a comparison with Li and K ion storage. *Carbon* 157, 316–323. doi: 10.1016/j.carbon.2019.10.045

Liu, H., Hu, Z., Tian, L., Su, Y., Ruan, H., Zhang, L., et al. (2016). Reduced graphene oxide anchored with δ-MnO2 nanoscrolls as anode materials for enhanced Li-ion storage. *Ceram. Int.* 42, 13519–13524. doi: 10.1016/j.ceramint.2016.05.144

Liu, M., Zhao, Q., Liu, H., Yang, J., Chen, X., Yang, L., et al. (2019). Tuning phase evolution of β-MnO2 during microwave hydrothermal synthesis for high-performance aqueous Zn ion battery. *Nano Energy* 64, 103942. doi: 10.1016/j.nanoen.2019.103942

Ming, F. W., Liang, H. F., Lei, Y. J., Kandambeth, S., Eddaoudi, M., and Alshareef, H. N. (2018). Layered MgxV2O5·nH2O as cathode material for high-performance aqueous zinc ion batteries. *ACS Energy Lett.* 3, 2602–2609. doi: 10.1021/acsenergylett.8b01423

Nam, K. W., Kim, H., Choi, J. H., and Choi, J. W. (2019). Crystal water for high performance layered manganese oxide cathodes in aqueous rechargeable zinc batteries. *Energy Environ. Sci.* 12, 1999–2009. doi: 10.1039/c9ee00718k

Pan, H., Shao, Y., Yan, P., Cheng, Y., Han, K. S., Nie, Z., et al. (2016). Reversible aqueous zinc/manganese oxide energy storage from conversion reactions. *Nat. Energy.* 1:16039. doi: 10.1038/nenergy.2016.39

Randau, S., Weber, D. A., Kötz, O., Koerver, R., Braun, P., Weber, A., et al. (2020). Benchmarking the performance of all-solid-state lithium batteries. *Nat. Energy* 5, 259–270. doi: 10.1038/s41560-020-0565-1

Soundharrajan, V., Sambandam, B., Kim, S., Alfaruqi, M. H., Putro, D. Y., Jo, J., et al. (2018). Na2V6O16·3H2O barnesite nanorod: An open door to display a stable and high energy for aqueous rechargeable Zn-ion batteries as cathodes. *Nano Lett.* 18, 2402–2410. doi: 10.1021/acs.nanolett.7b05403

Sun, T., Nian, Q., Zheng, S., Shi, J., and Tao, Z. (2020). Layered Ca0.28MnO2·0.5H2O as a high performance cathode for aqueous zinc-ion battery. *Small* 16:2000597. doi: 10.1002/smll.202000597

Tang, B., Shan, L., Liang, S., and Zhou, J. (2019). Issues and opportunities facing aqueous zinc-ion batteries. *Energy Environ. Sci.* 12, 3288–3304. doi: 10.1039/c9ee02526j

Tie, Z., Liu, L., Deng, S., Zhao, D., and Niu, Z. (2020). Proton insertion chemistry of a zinc-organic battery. *Angew. Chem. Int. Edit.* 59, 4920–4924. doi: 10.1002/anie.201916529

Wan, F., Zhang, L., Dai, X., Wang, X., Niu, Z., and Chen, J. (2018). Aqueous rechargeable zinc/sodium vanadate batteries with enhanced performance from simultaneous insertion of dual carriers. *Nat. Commun.* 9:1656. doi: 10.1038/s41467-018-04060-8

Wang, C., Zeng, Y., Xiao, X., Wu, S., Zhong, G., Xu, K., et al. (2020). γ-MnO2 nanorods/graphene composite as efficient cathode for advanced rechargeable aqueous zinc-ion battery. *J. Energy Chem.* 43, 182–187. doi: 10.1016/j.jechem.2019.08.011

Wang, D., Wang, L., Liang, G., Li, H., Liu, Z., Tang, Z., et al. (2019a). A superior δ-MnO2 cathode and a self-healing Zn-δ-MnO2 battery. *ACS Nano* 13, 10643–10652. doi: 10.1021/acsnano.9b04916

Wang, J., Wang, J.-G., Liu, H., Wei, C., and Kang, F. (2019b). Zinc ion stabilized MnO2 nanospheres for high capacity and long lifespan aqueous zinc-ion batteries. *J. Mater. Chem. A* 7, 13727–13735. doi: 10.1039/c9ta03541a

Wang, J., Wang, J.-G., Liu, H., You, Z., Wei, C., and Kang, F. (2019c). Electrochemical activation of commercial MnO microsized particles for high-performance aqueous zinc-ion batteries. *J. Power Sources* 438, 226951. doi: 10.1016/j.jpowsour.2019.226951

Wang, Y., Qu, Q., Gao, S., Tang, G., Liu, K., He, S., et al. (2019d). Biomass derived carbon as binder-free electrode materials for supercapacitors. *Carbon* 155, 706–726. doi: 10.1016/j.carbon.2019.09.018

Wang, F., Borodin, O., Gao, T., Fan, X., Sun, W., Han, F., et al. (2018). Highly reversible zinc metal anode for aqueous batteries. *Nat. Mater.* 17, 543–549. doi: 10.1038/s41563-018-0063-z

Wu, B., Zhang, G., Yan, M., Xiong, T., He, P., He, L., et al. (2018). Graphene scroll-coated alpha-MnO2 nanowires as high-performance cathode materials for aqueous Zn-ion battery. *Small* 14:1703850. doi: 10.1002/smll.201703850

Xie, X., Liang, S., Gao, J., Guo, S., Guo, J., Wang, C., et al. (2020). Manipulating the ion-transfer kinetics and interface stability for high-performance zinc metal anodes. *Energy Environ. Sci.* 13, 503–510. doi: 10.1039/c9ee03545a

Xu, W., Zhao, K., Huo, W., Wang, Y., Yao, G., Gu, X., et al. (2019). Diethyl ether as self-healing electrolyte additive enabled long-life rechargeable aqueous zinc ion batteries. *Nano Energy* 62, 275–281. doi: 10.1016/j.nanoen.2019.05.042

Yamamoto, T., and Shoji, T. (1986). Rechargeable Zn| ZnSO4| MnO2-type cells. *Inorg. Chim. Acta* 117, L27–L28.

Yang, Q., Mo, F., Liu, Z., Ma, L., Li, X., Fang, D., et al. (2019). Activating C-Coordinated iron of iron hexacyanoferrate for Zn hybrid-ion batteries with 10000-cycle lifespan and superior rate capability. *Adv. Mater.* 31:1901521. doi: 10.1002/adma.201901521

You, Z., Liu, H., Wang, J., Ren, L., and Wang, J.-G. (2020). Activation of MnO hexagonal nanoplates via in situ electrochemical charging toward high-capacity and durable Zn-ion batteries. *Appl. Surf. Sci.* 514:145949. doi: 10.1016/j.apsusc.2020.145949

Yu, F., Li, S., Chen, W., Wu, T., and Peng, C. (2019). Biomass-derived materials for electrochemical energy storage and conversion: Overview and perspectives. *Energy Environ. Mater.* 2, 55–67. doi: 10.1002/eem2.12030

Yuan, D., Manalastas, W. Jr., Zhang, L., Chan, J. J., Meng, S., Chen, Y., et al. (2019). Lignin@nafion membranes forming Zn solid-electrolyte interfaces enhance the cycle life for rechargeable zinc-ion batteries. *ChemSusChem* 12, 4889–4900. doi: 10.1002/cssc.201901409

Zhang, L., Chen, L., Zhou, X., and Liu, Z. (2015). Towards high-voltage aqueous metal-ion batteries beyond 1.5 V: The zinc/zinc hexacyanoferrate system. *Adv. Energy Mater.* 5:1400930. doi: 10.1002/aenm.201400930

Zhang, N., Cheng, F., Liu, J., Wang, L., Long, X., Liu, X., et al. (2017). Rechargeable aqueous zinc-manganese dioxide batteries with high energy and power densities. *Nat. Commun.* 8:405. doi: 10.1038/s41467-017-00467-x

Zhang, X., Wu, S., Deng, S., Wu, W., Zeng, Y., Xia, X., et al. (2019). 3D CNTs networks enable MnO2 cathodes with high capacity and superior rate capability for flexible rechargeable Zn-MnO2 Batteries. *Small Methods* 3:1900525. doi: 10.1002/smtd.201900525

Zhong, C., Liu, B., Ding, J., Liu, X., Zhong, Y., Li, Y., et al. (2020). Decoupling electrolytes towards stable and high-energy rechargeable aqueous zinc-manganese dioxide batteries. *Nat. Energy* 5, 440–449. doi: 10.1038/s41560-020-0584-y

Zhou, W., Chen, J., He, C., Chen, M., Xu, X., Tian, Q., et al. (2019). Hybridizing δ-type NaxV2O5·nH2O with graphene towards high-performance aqueous zinc-ion batteries. *Electrochim. Acta* 321:134689. doi: 10.1016/j.electacta.2019.134689

Conflict of Interest: The authors declare that the research was conducted in the absence of any commercial or financial relationships that could be construed as a potential conflict of interest.